Proc. of SPIE Vol. 3113, Grazing Incidence and Multilayer X-Ray Optical Systems, ed. R B Hoover, A B Walker (Jul 1997) Copyright SPIE

Focus and Alignment of the AXAF Optics

T. J. Gaetz[a], W. A. Podgorski[a], L. M. Cohen[a], M. D. Freeman[a], R. J. Edgar[a], D. Jerius[a], L. Van Speybroeck[a], P. Zhao[a],

and

J. Kolodziejczak[b], M. Weisskopf[c]

[a]Smithsonian Astrophysical Observatory, Cambridge, MA 02138 USA

[b]USRA/Marshall Space Flight Center, Huntsville, AL 35812 USA

[c]NASA/Marshall Space Flight Center, Huntsville, AL 35812 USA

ABSTRACT

We discuss the X-ray measurement of the focus and alignment of the AXAF (Advanced X-ray Astrophysics Facility) X-ray optics. The High Resolution Mirror Assembly (HRMA) consists of four nested Wolter type I X-ray optics. The attainment of the program goals for high resolution imaging requires that the mirror foci be coincident, both axially and laterally; in addition, the relative tilts between optics within each mirror pair must be small.

The mirror tilts and the parfocalization were measured at the X-Ray Calibration Facility (XRCF) at the Marshall Space Flight Center in Huntsville, Alabama during a series of tests in the winter/spring of 1996/1997. The X-ray measurements are compared to the optical alignment data obtained by Eastman Kodak using the HRMA Alignment and Test System (HATS) during HRMA assembly. From these data a preliminary model for the relative location and rigid-body orientation of the individual mirror elements is developed; this mirror model is a component of the SAO high fidelity HRMA raytrace model.

Keywords: X-ray optics, Wolter Type-I, AXAF, Alignment

1. INTRODUCTION

The alignment of the Advanced X-ray Astronomy Facility (AXAF) optics is an important part of attaining the objective of high resolution X-ray imaging. The HRMA consists of four nested Wolter Type-I mirror pairs; each mirror pair consists of a paraboloid (P) mirror and a matching hyperboloid (H) mirror. For historical reasons the mirror pairs (or shells) are numbered 1, 3, 4, and 6 from largest to smallest. In order to attain imaging goals, each mirror pair must be accurately aligned and focused, and in addition, the individual mirror pair foci must be aligned axially and laterally (axial and lateral parfocalization, respectively). In this paper we discuss the preliminary assessment of the focus and alignment of the AXAF High Resolution Mirror Assembly (HRMA) based on optical alignment measurements during HRMA assembly, X-ray measurements of focus and tilt, off-axis X-ray images, and high fidelity raytrace modeling. In §2 we describe the data obtained optically at Eastman Kodak (EKC) and in X-rays at the X-ray Calibration Facility (XRCF). In §3 we discuss the analysis of the optical and X-ray data and derive estimates for the coma, lateral and axial parfocalization, and the (coma-free) tilt-compensated decenter. In §4 we describe the SAO high fidelity raytrace model used in the analyses and the updates to the rigid body parameter specification. Finally, in §5 we summarize the AXAF HRMA alignment.

Other author information: (Send correspondence to T.J.G.)
T.J.G.: Email: tgaetz@cfa.harvard.edu; Telephone: 617-496-7584; Fax: 617-495-7356

2. ALIGNMENT DATA

2.1. Coordinates

In the following we use "XRCF coordinates" (see Figure 1). In this system, the X–axis is the optical axis with X increasing from the detector towards the X-ray mirrors. The Z–axis is *up*, and the Y–axis completes a right-handed coordinate system; at XRCF, $+Y$ is towards *south*. The coordinate origin is taken to be coincident with the intersection of the nominal optical axis with the plane defined by the P side of the HRMA Central Aperture Plate (CAP datum A). (The CAP is the central structural support plate between the P and H optics.) The optic tilt conventions are:

tilt$_Y$: positive rotation about an axis parallel to the XRCF $+Y$ axis.
tilt$_Z$: positive rotation about an axis parallel to the XRCF $+Z$ axis.

Off-axis directions are specified in terms of HRMA *pitch* and *yaw*:

pitch: positive rotation about an axis parallel to the XRCF $+Y$ axis.
yaw: positive rotation about an axis parallel to the XRCF $+Z$ axis.

In all cases, a positive rotation is right-hand-rule rotation, *i.e.*, $+X$ towards $+Y$, $+Y$ towards $+Z$, or $+Z$ towards $+X$.

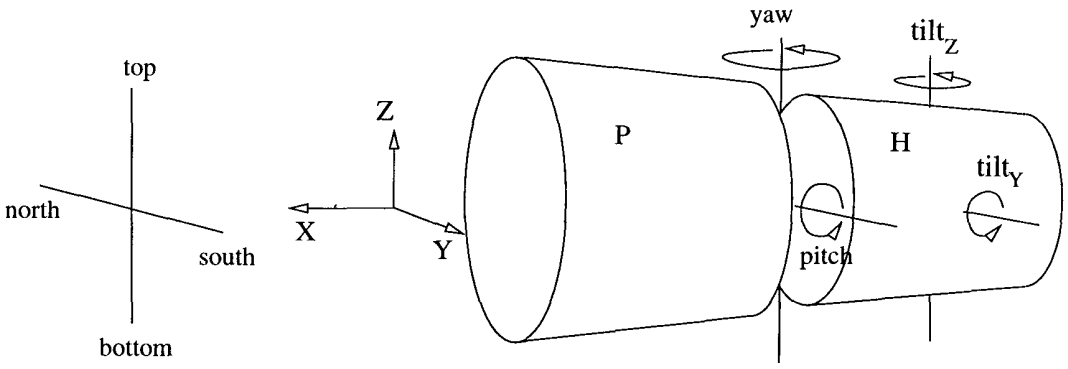

Figure 1. Schematic of XRCF coordinates

2.2. HRMA alignment measurements at Eastman Kodak Company

During HRMA buildup, the alignment state of the HRMA optics was assessed using the EKC HRMA Alignment Test System (HATS). In this configuration the HRMA optics were supported vertically in an assembly and testing tower (H optics upper, P optics lower) suspended above an Autocollimating Flat (ACF). An aperture mask with 24 evenly spaced apertures for each test zone (*i.e.*, mirror pair) was placed above the ACF; the aperture mask also carried a Tilt Reference Indicator (TRI). The TRI consists of a pair of autocollimators, one looking down at the ACF, and the other looking up at the Alignment Reference Mirror (ARM) mounted in the CAP; the TRI monitored the parallelism between the CAP and the ACF. The ARM also provided an axial reference. HATS includes a Centroid Detector Assembly (CDA) mounted on rails at the top of the tower; this was used to assess the alignment of the optics at the 20 m (folded path) P focus or at the 10 m system focus. The alignment of the HRMA was probed using a double-pass system in which a directable laser beam was reflected off an H, a P, the ACF, the P and H again, finally reaching a detector back at the centroid detector; the centroids of the returned beam and an internal reference beam were measured using a quad-cell detector.

The alignment test is basically a double-pass Hartmann test of the X-ray optics; the variation in the return beam centroid location with azimuth around the optic can be used to assess the on-axis coma and parfocalization of the system. For a given mirror pair, the HATS measures the double-pass centroids for a set of 24 apertures equally spaced in azimuth around the optic. A Fourier transform of these data is performed and the low-order terms are

interpreted in terms of rigid-body misalignments. For a double-pass configuration containing both a P optic and its corresponding H optic, the Fourier terms relevant to rigid-body alignment are

Fourier Coefficient	Rigid Body Term
$Re\,(Q_0)$ and $Im\,(Q_0)$	lateral focus error
$Re\,(Q_1)$	axial focus error
$Re\,(Q_2)$ and $Im\,(Q_2)$	coma

where Q_n is the Fourier coefficient of order n, and Re and Im indicate the real and imaginary components, respectively. Basically, Q_0 gives the displacement of the image in the focal plane, $Re\,(Q_1)$ gives the radius of the cone of rays (positive in front of the focal point, negative behind the focal point), and Q_2 provides the size and orientation of the coma circle. Because this is a double-pass experiment, the actual parfocalization and coma errors are a factor of two smaller than the Q_n coefficients. Although the interpretation of the HATS Q_0 and Q_2 Fourier coefficients is straightforward, the interpretation of Q_1 is complicated by a number of axially symmetric biases including deformation of the CAP under load, curvature of the ACF, "dimples" induced by the mirror supports under 1g, and refraction by radial air temperature gradients within the HRMA.

Final HATS ATP (Acceptance Test Procedure) data consisted of 9 tests performed on November 9 and 10, 1996; these were augmented with an additional 15 tests performed at that time. A Fourier decomposition was performed for each of the 24 tests. The means and standard deviations were evaluated for this set of Fourier coefficients; the coefficients relevant to rigid-body mirror element alignment are given in table 1. The quoted errors are the standard deviations for the set of 24 Fourier decompositions. The HATS test procedure yields only relative values for the parfocalization so $\langle Q_0 \rangle = [-5.48, 9.42]$, the R^2-weighted mean, was subtracted from Q_0; R is an effective radius for the mirror pair. The Q_1 coefficients are given relative to the value of Q_1 for mirror pair 3.

Table 1. HATS ATP (Augmented) Fourier Coefficients.

	Coefficient	units	MP1	MP3	MP4	MP6
1	$Re\,(Q_0 - \langle Q_0 \rangle)$	(μm)	-5.97 ± 9.42	5.30 ± 9.40	4.17 ± 9.66	1.69 ± 9.24
2	$Im\,(Q_0 - \langle Q_0 \rangle)$	(μm)	-1.71 ± 8.89	4.10 ± 8.77	0.57 ± 9.00	-4.43 ± 9.08
3	$Re\,(Q_1(\mathrm{MPN}) - Q_1(\mathrm{MP3}))$	(μm)	-12.67 ± 1.09	0.00 ± 2.42	-18.69 ± 1.35	18.79 ± 1.94
4	$Re\,(Q_2)$	(μm)	-8.66 ± 0.35	6.26 ± 0.58	5.76 ± 0.27	29.68 ± 0.62
5	$Im\,(Q_2)$	(μm)	2.60 ± 0.30	-1.93 ± 0.59	-0.76 ± 0.38	-3.07 ± 0.44

2.3. HRMA alignment measurements at XRCF

A large number of X-ray measurements were performed at the X-Ray Calibration Facility (XRCF) at the Marshall Space Flight Center and these data are currently being analyzed. The measurements most directly relating to assessment of the rigid-body alignment are a series of *quadrant shutter focus measurements* which had the aim of measuring the HRMA parfocalization and on-axis coma. The X-ray source was at a distance of approximately 527300 mm from the HRMA CAP (midway between the P and H optics). In these focus and tilt measurements, the X-ray source was an electron impact point source (EIPS) with an Al target; all the X-ray data used here was taken at the Al Kα line. Quadrant shutters between the HRMA and the detector allowed individual mirror pair quadrants to be isolated. The detector was a flow proportional counter; a 20 μm moveable pinhole in front of the detector was used to map out the beam in order to measure the centroid of the X-ray image.

Off-axis images taken with the High-Speed Imager (HSI, a microchannel-plate detector) have proven to be a sensitive probe of tilt-compensated decenter misalignments; the optical measurements of Q_0, Q_1, and Q_2 were insensitive to this form of misalignment.

The quadrant shutter focus procedure uses a combination of the centroids of the X-ray beam as seen through a individual mirror quadrant; because of overlap by adjacent quadrant shutter blades, the actual opening angle for a

quadrant is about 88°. The four quadrants are labeled *Top*, *North*, *Bottom*, and *South* (named after the directions at the XRCF; see Figure 1). Quadrant shutter measurements for an individual mirror pair yield four pairs of centroid coordinate values. From these two focus estimates can be constructed:

$$\Delta_{Y,i} = 0.995\frac{\pi}{4\sqrt{2}}\frac{F}{R_i}(Y_{i,N} - Y_{i,S}), \qquad \Delta_{Z,i} = 0.995\frac{\pi}{4\sqrt{2}}\frac{F}{R_i}(Z_{i,T} - Z_{i,B}), \tag{1}$$

where $\Delta_{Y,Z}$ are the focus error estimates; R_i is the nodal radius for the mirror pair, and F is the distance from the mirror node to the (finite conjugate) focus. (The 0.995 factor accounts for the fact that the quadrants are really only 88°.) A disagreement between these two focus error estimates may be indicative of astigmatism, either intrinsic in the optic or resulting from 1g distortions. In addition, two alignment estimators can be formed:

$$tilt_{Y,i} = 0.978\frac{\pi}{4F_i'}(Y_{i,N} + Y_{i,S} - Y_{i,T} - Y_{i,B}), \qquad tilt_{Z,i} = 0.978\frac{\pi}{4F_i'}(Z_{i,N} + Z_{i,S} - Z_{i,T} - Z_{i,B}), \tag{2}$$

where F_i' is the distance from the body center of the H optic to the *far focus* of the H. (The 0.978 factor is a correction for 88° quadrants.) Note that these estimators may be biased by the tilt-compensated decenter of the optics (see below); preliminary raytrace investigations indicate that the focus error estimators are not significantly biased, but the tilt estimators may be biased. In any event, we compare the measurements to simulations containing the effects of the tilt-compensated decenters so any biases will appear in both the simulations and the measurements.

Measurements were performed quadrant by quadrant for individual mirror pairs as well as for the HRMA as a whole. The centroids of the quadrant images were measured by performing two-dimensional pinhole scans (normally a 7×7 array with a 20 μm pinhole on 20 μm centers). Measurements were taken on three separate occasions during Phase 1 of the XRCF testing: an initial dataset (D-66), an intermediate dataset (D-67), and the final dataset (E-67). The most reliable dataset was the last one taken: more was known about the mirror pair image qualities beforehand and more time was allocated to sample the full image from each quadrant of each mirror pair. The quadrant image centroids measured from these scans can be used to estimate the best focus position of each of the four HRMA mirror pair (§3.3) as well as the on-axis coma (§3.1).

3. ANALYSIS OF ALIGNMENT MEASUREMENTS

3.1. Coma

Rigid body misalignments of the P to H optics in either decenter or tilt can cause a comatic image distortion in the focal plane. The size of the coma circle in the focal plane is related to a pure H relative decenter or a pure H relative tilt angle as:

	1″ H tilt	1 mm H decenter
Coma circle radius (″)	1	10
Coma circle radius (μm)	48.5	488

The breakdown between mirror element tilt and decenter is not uniquely determined by the coma as measured on-axis. Because both tilt and decenter introduce coma, the net coma can vanish for some combination movements; in particular, for combinations of H tilt + H decenter which are equivalent to a pure rotation about the H far focus, the comas introduced by the decenter and the tilt cancel each other leaving the net coma unchanged. We therefore factor the decenter and tilt into two components:

- coma; appears even on-axis
- tilt-compensated decenter; no on-axis coma is produced, but an additional off-axis aberration appears (see §3.4)

We interpret the coma as a pure body-centered tilt of the H relative to its companion P optic. (This also introduces a lateral shift of the image; this is removed by applying a decenter to the mirror pair as a whole.) In the rest of this section, *tilt* refers to the corresponding component of on-axis coma expressed as a tilt of the H optic unless otherwise noted. Note also that the relation between angular measure and linear measure in the focal plane is 1″ ~ 48.8 μm.

Table 2. HRMA On-Axis Coma

	Model	Shell 1		Shell 3		Shell 4		Shell 6	
		Y ["]	Z ["]	Y ["]	Z ["]	Y ["]	Z ["]	Y ["]	Z ["]
1	Kodak HATS ATP (augmented)	0.03	-0.09	-0.02	0.07	0.00	0.06	-0.03	0.32
2	XRCF 1g Correction (SAO)	-0.24	0.00	-0.08	0.00	-0.12	0.00	-0.12	0.00
3	XRCF 1g Correction (EKC)	-0.23	0.00	-0.18	0.00	-0.21	0.00	-0.33	0.00
4	XRCF Data 1/5-6/97†	-0.15	-0.14	-0.05	-0.06	-0.04	-0.08	-0.44	0.18
5	XRCF Data 1/5-6/97†	-0.17	-0.14	-0.07	-0.05	-0.05	-0.07		
6	Off-axis yaw correction	0.00	0.15	-0.01	0.18	0.01	0.19	0.00	0.20
7	XRCF Data 1/5-6/97 (+ yaw corr.)	-0.15	0.01	-0.06	0.12	-0.03	0.11	-0.44	0.38
8	XRCF Data 2/7-8/97	-0.14	-0.02	-0.05	0.12	-0.04	0.04	-0.43	0.36
9	Current Model (EKCHDOS06/SAO)	-0.01	-0.03	0.13	0.11	0.04	0.15	-0.05	0.38
10	Data - Model ([9] - [8])	-0.13	0.01	-0.18	0.01	-0.08	-0.11	-0.38	-0.02

†XRCF tilts measured $-1'$ off-axis in yaw

Table 2 provides a summary of the on-axis coma as estimated by several methods. The Kodak HATS measurements (HATS ATP augmented test set, see Table 1) provided the first post-assembly estimate for the coma; the HATS value (converted to equivalent H-optic tilt) is listed in line 1 of Table 2. In lines 2 and 3 the XRCF 1g *corrections* to the tilt angles are given for both the SAO and the EKC finite element models; note that the corrections are about XRCF Y only, Y being the horizontal axis at XRCF. Lines 4 and 5 present data from quadrant shutter X-ray tests done January 5-6, 1997 when the HRMA was $\sim 1'$ off-axis in yaw; line 4 is the initial baseline tilt data from these tests, and line 5 is repeatability data in which the *top* quadrant was re-measured and used in conjunction with the initial data from the other three quadrants; if the experiment is working correctly, lines 4 and 5 should be the same. Line 6 gives the correction between the $1'$ off-axis condition of the HRMA during the 1/5-6/97 tests and the on-axis configuration.

Line 7 is the arithmetic sum of lines 4 and 6, *i.e.*, the 1/5-6/97 data corrected to 0 yaw. This can be compared directly to line 8, the results from the last (E-67) series of Al Kα focus/tilt measurements in Phase 1, taken on 2/7/97 and 2/8/97. The agreement is excellent: the $1'$ difference in yaw explains the difference between the 1/5-6/97 and 2/7-8/97 measurements.

The measurements can now be compared to a model based on our current best estimate of the rigid body parameters as derived from the X-ray and optical data (line 9). Finally, line 10 lists the differences between the 2/7-8/97 measurements (line 8) and the model (line 9). The differences are generally small, but the differences in $tilt_Y$ are systematically larger; these differences may indicate a lack of accuracy in the modeling the XRCF 1g effects: by symmetry only $tilt_Y$ should be affected by gravity in the XRCF testing configuration.

3.2. Lateral parfocalization

The focal plane image decenter (lateral parfocalization) estimates based on the HATS ATP (extended) data are given in Table 3. Because HATS is a double-pass test, Q_0 from Table 1 is actually twice the lateral parfocalization error.

Table 3. Lateral Parfocalization (μm); $1'' \sim 48.8\,\mu$m in the focal plane

		MP1	MP3	MP4	MP6
1	ΔY	3.00 ± 4.71	-2.65 ± 4.70	-2.08 ± 4.83	-0.84 ± 4.62
2	ΔZ	-0.86 ± 4.44	-2.05 ± 4.38	-0.28 ± 4.50	-2.22 ± 4.54

Analysis of the X-ray data bearing on lateral parfocalization is still in progress. Measurement of the lateral parfocalization in X-rays is complicated by several factors: tilts induced by 1g distortion of HRMA as supported in the horizontal XRCF configuration, maintaining stability and accuracy of absolute centroid positions over long timescales, and the large pinholes (10 μm or 20 μm). Although the X-ray measurements may not improve on the HATS

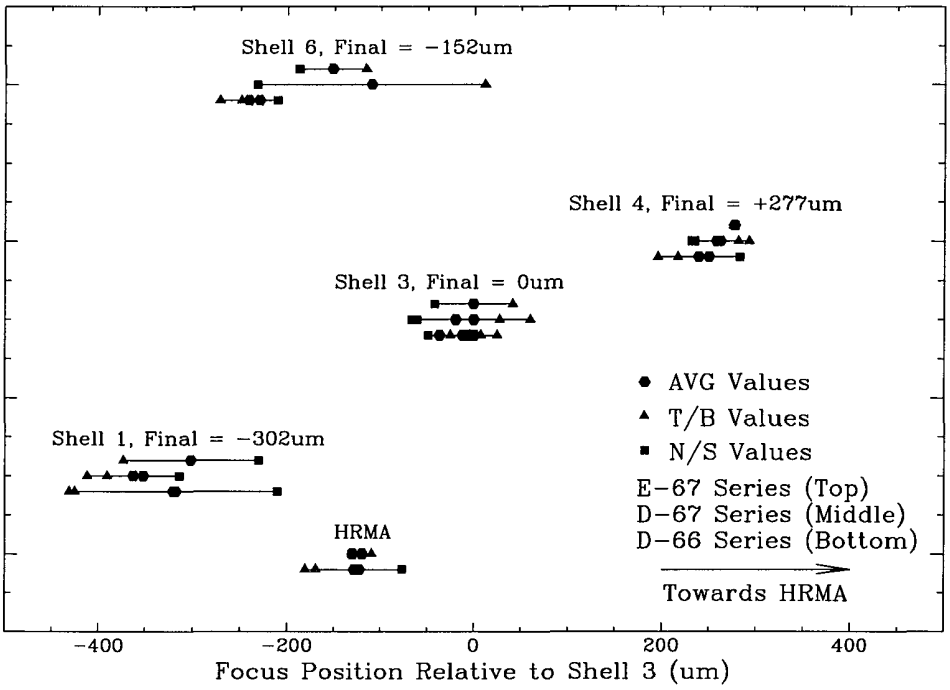

Figure 2. HRMA Focus Data. Focal positions are given in μm and are measured relative to the mirror pair 3 focus; a positive difference represents a focus position closer to the HRMA than the Shell 3 focus. The data are from three series of tests and are shown stacked – the legend describes the stacking order. Note that there were no HRMA tests in series E-67.

values, the X-ray centroids will provide additional constraints on the 1g model. (In the optical HATS measurements the HRMA was supported vertically, so no appreciable 1g-induced tilts are introduced.)

3.3. Axial parfocalization

We have analyzed data for the "quadrant shutter focus" two-dimensional pinhole scans; the X-Ray focus data from the three sets of quadrant shutter focus data sets (D-66 series, D-67 series, and E-67 series) are summarized in Figure 2. Two focus estimators are available from the quadrant centroids (Eq. 1): the difference in the Z centroids of the *top* and *bottom* quadrant images, and the difference in the Y centroids of the *north* and *south* quadrant images. The average of these two estimators is used as the focus estimate. A difference between the T/B focus and the N/S focus may be due to either astigmatism in the mirrors or to measurement error; a certain amount of separation is also induced by the 1g test environment. Raytrace simulation indicates that the coma-free tilt-compensated decenter (§3.4) does not bias this focus estimate.

As noted above, the best focus dataset was the last one taken (E-67; top line of each grouping); more was known about the mirror pair image qualities beforehand and more time was allocated to capture all of the flux from each quadrant of each mirror pair. These data are also preferred over the optical (HATS) measurements because of difficult-to-evaluate axially symmetric biases in the Tower environment; in particular, the X-ray tests were in vacuum so all problems with refraction by air temperature gradients are avoided.

The relative foci from the last set of X-ray measurements are shown in Table 4. Again, positive numbers represent focus positions closer to the HRMA, *i.e.*, shorter overall focal lengths.

In Figure 3 the XRCF measured focus data are compared with various focus predictions for both the on-orbit (infinite source distance) and XRCF (finite source distance) conditions. As in Figure 2, the abscissa shows the difference between the Shell N focus and the Shell 3 focus with a positive difference indicating a focus value *towards*

Table 4. Focus of Shells relative to Shell 3: $F_N - F_3$

		units	MP1	MP3	MP4	MP6
1	HATS On-orbit Prediction 11/96	(μm)	+52	0	+220	−292
2	X-ray Data 2/7-8/97	(μm)	−302	0	+277	−152
3	Model EKCHDOS06/SAO(XRCF)	(μm)	−305	0	+274	−144
4	On-orbit Prediction	(μm)	−42	0	+277	−174

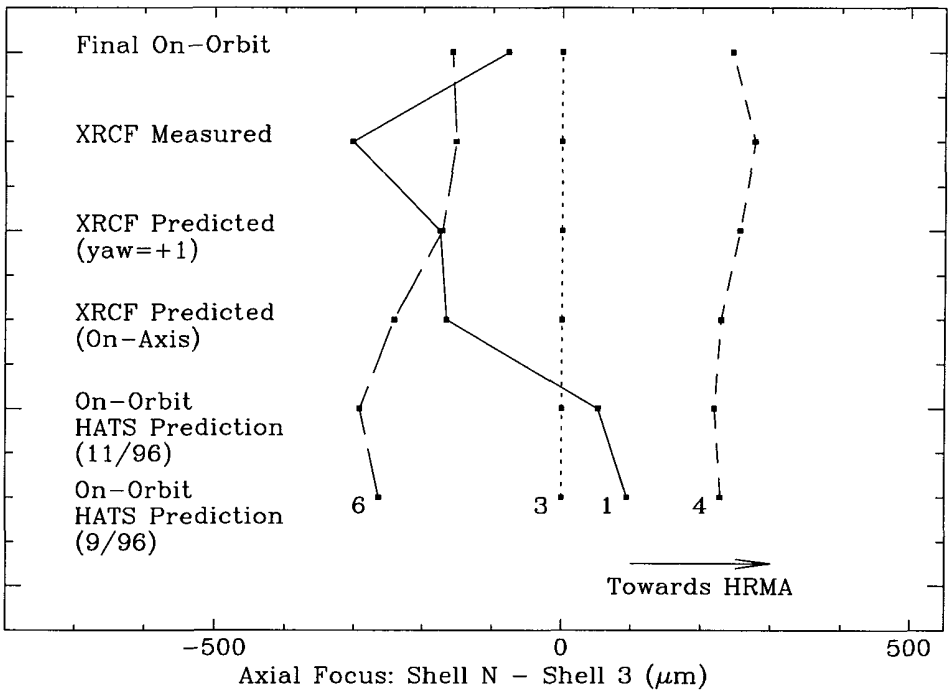

Figure 3.

the HRMA relative to Shell 3. Six different cases are shown, presented vertically with the focus values (dots) of each mirror pair connected by lines. The bottom two cases represent the predictions of *on-orbit* focus based on the Kodak HATS data. The bottom set of data is from the September 96 testing, taken after all mirror alignments were completed but prior to HRMA final assembly. The next set represents an estimate from Kodak's November 96 HRMA ATP data set taken following the HRMA final assembly at Kodak and just prior to shipment to XRCF. Both sets of data show that the foci of the mirror pairs span about 500 μm, with the foci ordered as (6 – 3 – 1 – 4) in order of *decreasing* focal lengths.

The middle two cases in Figure 3 represent predictions of XRCF focus from the 11/96 Kodak test data, for HRMA yaw angles of both 0′ and 1′. Table 4 includes predictions for focal points relative to the mirror pair 3 focus both for infinite (on-orbit) source distance and finite (XRCF) source distance. The overall change in focal distance is about 195mm between on-orbit and XRCF (longer at XRCF); an interesting feature is that the focal distance for Shell 1 increases much more (about 250 μm) than for the other 3 mirror pairs. This can also be seen in Figure 3 as the Shell 1 focus moves from a position between 3 and 4 (on-orbit case) to a position between 6 and 3, further away from the HRMA. This behavior, initially considered to be an anomaly and possibly an error, is now understood; the as-built mirror axial spacings plus the P1 and H1 surface prescriptions give this result.

The "XRCF measured" case in Figure 3 presents what is considered to be the best current estimate from XRCF testing of shell-to-shell relative focus; this is the the data from Table 4 (line 2) discussed above. We see that there

is is a discrepancy of about 200 μm in the position of the Shell 1 focus at XRCF as compared with the predictions based on Kodak optical test data. At XRCF, Shell 1 had the longest focal distance, a result which was consistent over all of the testing. Because of axially symmetric biases present in the HATS axial focus determination, it was decided that the XRCF focus data was most likely more accurate; we used the XRCF-determined axial foci data as the basis for our HRMA raytrace model. Our best current raytrace model for the final on-orbit foci is shown as the top case in Figure 3; the mirror maps were equivalent to the current best XRCF mirror maps except that the 1g effects were omitted. This predicted HRMA on-orbit performance is somewhat better than the XRCF measurement – the span of the foci is reduced.

The mirror dimensions were measured mechanically by Hughes Danbury Optical Systems (HDOS) and EKC. The distance of the end of each P optic from CAP Datum A (P side of the CAP) and the distance of each H optic from CAP Datum D (H side of the CAP) were mechanically gauged; these mechanical measurements of the mirror axial positions are believed to be more accurate than our knowledge of the mirror cone angles. A cone angle correction was applied to the mirror maps in order to make the raytrace (XRCF) foci agree with the values in line 2 of Table 4; the values obtained from the current raytrace model are given in line 3 of that table. Line 4 gives a preliminary estimate of the on-orbit axial parfocalization.

3.4. Tilt-compensated decenter (coma-free)

The presence of a tilt-compensated decenter in the AXAF optics was originally deduced on the basis of quadrant shutter flux measurements and confirmed by analysis of off-axis X-ray images. Tilt-compensated decenter is a form alignment error in which the coma from an optic decenter is canceled out by a compensating tilt of the optic; it does not affect the on-axis on-orbit coma, but produces an additional off-axis aberration.

The magnitude and direction of the decenter can be quite well constrained by the available off-axis images. The lower right panel of Figure 4 shows an example of an off-axis image for mirror pair 1 ($pitch = 0', yaw = -20'$). The off-axis images show two large approximately oval lobes; these are a facility effect resulting from the spherical aberration which is introduced by the finite source distance at XRCF. Symmetry considerations indicate that for an ideal perfectly aligned telescope, these lobes should be symmetric about a line containing the off-axis image and the optical axis. The observed large lobes are asymmetric and also tilted relative to each other; this is a consequence of the tilt-compensated decenter within the mirror pair. The lighter swathes through the image result from shadowing by support struts, predominantly those in the Central Aperture Plate. The approximately concentric ripples in the large lobes result from the low-order mirror surface errors. These are also caustics, analogous to the pattern of bright lines on the bottom of a swimming pool caused by the ripples on the water surface; in this case they result from axial ripples on the mirror surface. The agreement between the location and shape of the ripples in the X-ray data as compared to the raytraces is an indication of the fidelity of the low-order mirror maps used in the raytrace.

In addition to the offsets in the large lobes, a relative P to H decenter produces a pincushion-shaped caustic at best focus; raytrace studies show that the size of the pincushion scales inversely with mirror pair radius and increases with magnitude of off-axis angle (at constant decenter) and also increases with magnitude of the decenter (at constant off-axis angle). For fixed magnitude of off-axis angle and decenter, the orientation of the axes of the pincushion varies with the relative angle between off-axis direction and the decenter direction; very approximately, when the angle of the decenter relative to the off-axis direction changes, the pincushion orientation changes by about half that amount.

For constant off-axis angle and in the neighborhood of a given decenter+tilt value, the variation of the pincushion size with decenter magnitude and the variation of pincushion orientation with decenter direction are relatively uncoupled. Comparison of the ($pitch = 0', yaw = -20'$) images with raytraces allowed the decenter magnitude and direction to be estimated. The size and orientation of the pincushions were measured in the X-ray images and sensitivities obtained from the raytraces were used to refine the decenter estimates. The upper left panel of Figure 4 shows the results of our current best raytrace model incorporating the (tilt-compensated) decenter values listed in Table 5. The raytrace models do not incorporate a strong angle-dependent quantum efficiency factor in the HSI detector and vignetting by the quadrant shutter assembly, so the images are expected to differ in detail; nevertheless it is evident that the raytrace model produces good agreement in the dimensions and orientation of the pincushion feature. The other two panels in Figure 4 show the dependence on decenter direction and magnitude. In the upper right panel the decenter *magnitude* is increased by about 20%; the pincushion is noticeably larger. In the lower left

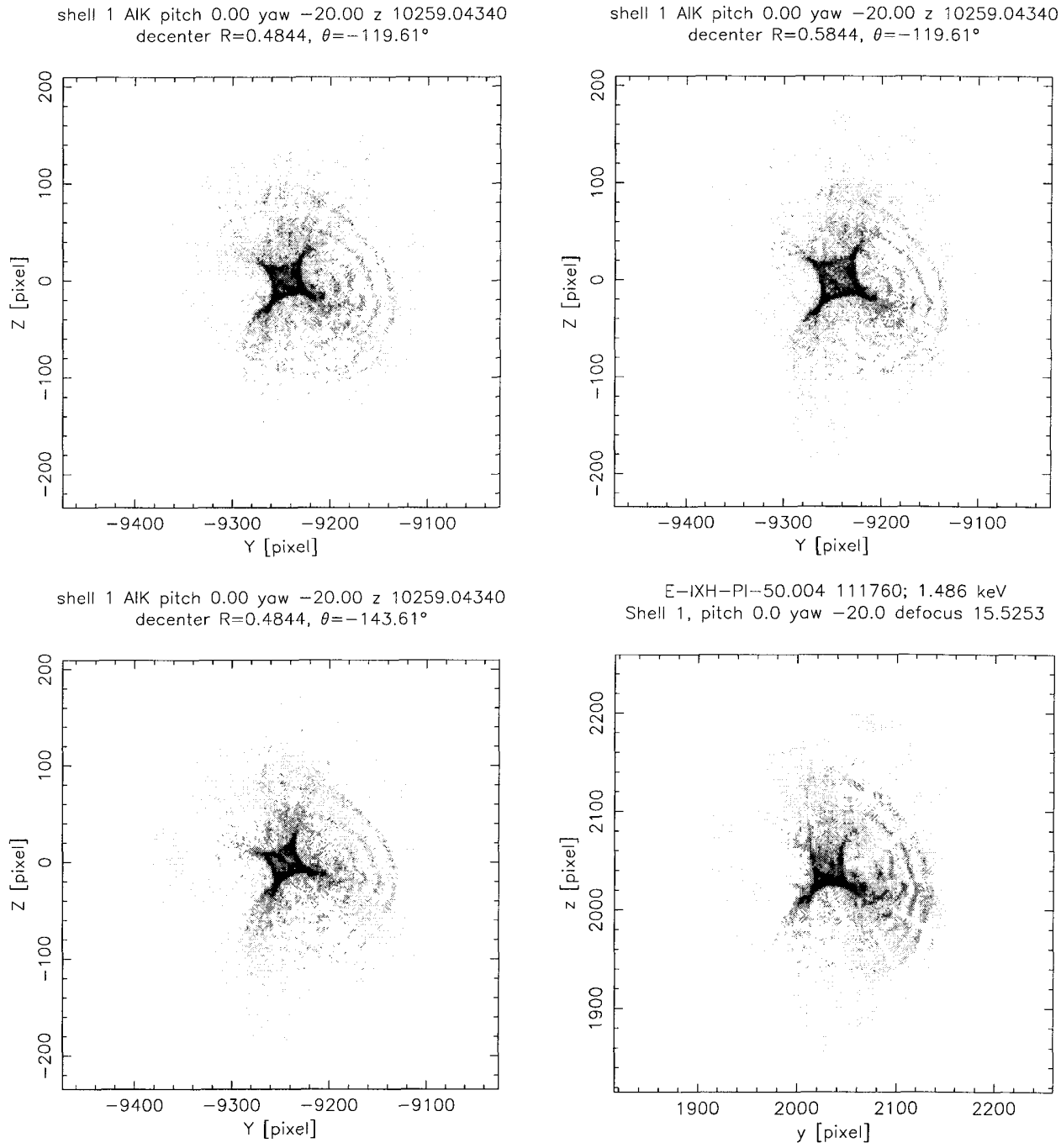

Figure 4. Off-axis images (Shell 1; *pitch* = 0′, yaw = −20′). Top left: Current best raytrace model. Top right: decenter *magnitude increased* by 0.1 mm. Bottom left: decenter *direction* changed by −24°. Bottom right: HSI image (X-ray data; to same scale as raytraces). Pixel width 6.43 μm; binned to 2×2 pixels. Logarithmic stretch. Note that these figures include gravity-induced distortions, spherical aberration introduced by the finite source distance, and other facility effects; they do *not* represent on-orbit performance.

panel the decenter *direction* is changed by 24°; the pincushion shows a noticeable rotation. We believe that the tilt-compensated decenter has been measured to better than 10%; further analysis of the data will refine the values and error estimates for the decenter parameters.

The estimated decenters of the H mirrors relative to their mating P mirrors are given in Table 5.

Table 5. H decenters relative to P optic

	decenter†		decenter†	
mirror	magnitude (mm)	angle from $+Y$ (°)	ΔY_H (mm)	ΔZ_H (mm)
H1	0.4844	−60.39	0.2393	−0.4211
H3	0.5077	−70.39	0.1704	−0.4782
H4	0.4562	−68.10	0.1702	−0.4233
H6	0.4736	−65.58	0.1958	−0.4312

†coma from decenter cancelled by compensating tilt

4. SAO HIGH FIDELITY RAYTRACE MODEL

A vital component of our analysis of the data and the eventual prediction of on-orbit performance is the high resolution raytrace model developed at SAO. The raytrace model is based in part on a NASA raytrace program (`OSAC`, written by Perkin-Elmer); portions of the `OSAC` code have been adapted, extended, and incorporated into our raytrace pipeline; a short description of an earlier version of the SAO raytrace architecture is given in Ref. 1.

The AXAF mirror elements were polished and figured by Hughes Danbury Optical Systems (HDOS). The HDOS mirror metrology was processed into a low-frequency mirror map (based on PMS axial scan data and CIDS circularity data) and high frequency errors (based on WYKO measurements). These data were split into two pieces and processed into a mirror map for low-frequency errors (modeled using 2D splines) and high frequency components (treated statistically as a scattering component).

Other low-frequency mirror distortions were modeled using high resolution finite element models; these include 1g gravitational distortions for the optics in various orientations: vertical during HRMA buildup and alignment at Eastman Kodak Company, and horizontal at the X-ray Test Facility (XRCF). The mechanical supports for the mirrors also introduce mirror distortions, notably a dimpling resulting from shrinkage of the epoxy bonding the mirror support pads to the mirrors. The 1g effects vanish on-orbit, but epoxy shrinkage and thermal gradients will still introduce distortions on-orbit. The mirror supports are lined up with the Central Aperture Plate (CAP) struts, so the largest-amplitude portion of the epoxy-shrinkage distortions are shadowed by support struts.

The surface deformations are modeled with high resolution 2D splines; the capability of using Fourier-Legendre coefficients has been retained for studies of low-order deformations. An SAO program, `addcases`, allows mirror deformations of various types to be added together into a single spline fit per surface; in this way the combined effects of intrinsic mirror deformations (based on metrology), deformations induced by mirror supports, and 1g distortions can be modeled. The HRMA XRCF mirror maps currently include:

- HDOS metrology; low frequency mirror map.
- deformations from SAO XRCF 1g mechanical model.
- epoxy shrinkage effects at +2 weeks.
- Assembly strains (estimated from HATS 2nd and 3rd order residuals).
- Cone angle corrections based on XRCF-measured axial parfocalization (see §3.3).

The HRMA on-orbit mirror maps are currently the same as the XRCF mirror maps except that the 1g mechanical distortions are omitted. Other model components are

- Central Aperture Plate (CAP), fore and aft structures, and P6 (ghost) baffle: modeled as annuli with rectangular struts; infinitely thin axially except for the CAP, which has the as-measured thickness.
- Scattering: surface microroughness derived from HDOS high-order surface maps (970220 version of scattering tables).
- Iridium optical constants: Henke 1995* values below 2 keV, SAO/MST Synchrotron group Ir reflectivity data for a P6 witness flat above 2 keV. (Currently reflection from a semi-infinite layer is modeled.)
- Finite source distance: 527279 mm at XRCF; 10 m or 20 m for the EKC Tower; the source is currently modeled as a monochromatic point source.

In this paper, when we compare experimental data to the "EKCHDOS06" model, the above SAO raytrace model (as updated in §4.1) is the one meant.

4.1. Rigid body parameters and SAO raytrace model update

In this section we briefly summarize the the current SAO raytrace model (`xrcf_SA01G+HDOS_HDOS-scat-970220_03`). The current rigid body misalignment model (`EKCHDOS06`) is an update based on the optical and X-ray measurements reported in this paper. This model is our current best model; however, it is still preliminary and will be further modified as improved data reductions and analyses become available. The `EKCHDOS06` rigid body model specifies the mirror following element positional data:

Mirror Spacing The mirror element spacing was based on mechanical measurements by EKC of the distance from the end of the optic to the corresponding face of the Central Aperture Plate. Together with the measured length of the optic, this determines the axial position of the mirror center.

Tilts (coma) The on-axis coma was evaluated from the EKC HATS ATP data (augmented by an additional 15 tests). The coma was assigned to pure tilt of the H mirror element relative to its companion P mirror element (§3.1).

Decenter (lateral parfocalization) The H tilt introduced above also causes a lateral focus shift. This was corrected by decentering the mirror pair as a whole to restore the lateral parfocalization as determined from the HATS ATP (augmented) measurements (§3.2).

Tilt-Compensated Decenter (coma-free) The far off-axis X-ray images revealed that some coma-free decenter is present in the HRMA. This was modeled by adding additional decenters to the H optics plus compensating tilts. The combined additional decenter plus compensating tilt is equivalent to a pure rotation of the H optic about its far focus (§3.4).

In addition, the mirror maps have been adjusted by small cone-angle corrections to make the relative X-ray axial focus positions consistent with the XRCF measured values (§3.3).

5. SUMMARY

5.1. HRMA alignment

This paper has presented the results of a first cut at analyzing the optical alignment data and the X-ray calibration data obtained at the XRCF. Our preliminary estimates for the on-axis coma and the axial and lateral parfocalizations as determined from the measurements are summarized in Table 7. The coma and the lateral parfocalization are based on the augmented HATS ATP data; the axial parfocalization is based on the 2/7-8/97 X-ray quadrant shutter focus measurements at XRCF.

Based on the above on-axis coma and parfocalization values and the coma-free tilt-compensated decenter values in Table 5, rigid body misalignments were incorporated into the baseline SAO raytrace model (see §4.1). To summarize: The on-axis coma was interpreted as pure body-centered H tilts. The tilt-compensated decenter was applied as a rigid-body rotation of the H about the H far focus. The lateral parfocalization was restored by a decenter of the

*Henke *et al.* 1993 plus updates; see Ref. 2 and `http://www-cxro.lbl.gov/optical_constants/`

Table 6. Mirror Body Center Coordinates (XRCF coordinate system)

Mirror	X (mm)	Y (mm)	Z (mm)	$tilt_Y$ (″)	$tilt_Z$ (″)
P1	426.5761	−0.1239	0.2151	0.0	0.0
P3	436.7098	−0.08675	0.2437	0.0	0.0
P4	440.3572	−0.08634	0.2168	0.0	0.0
P6	445.0821	−0.08625	0.2245	0.0	0.0
H1	−481.0146	0.1154	−0.2060	2.4194219	4.4454479
H3	−480.9282	0.08365	−0.2345	1.8542174	4.9943249
H4	−480.8279	0.08386	−0.2065	1.8468078	4.4350269
H6	−479.2152	0.1096	−0.2067	2.3720568	4.4891913

Table 7. Summary: HRMA Parfocalization and On-Axis Coma

		units	MP1	MP3	MP4	MP6
Lateral Parfocalization	ΔY	(μm)	3.00	−2.65	−2.08	−0.84
Lateral Parfocalization	ΔZ	(μm)	0.86	−2.05	−0.28	−2.22
Axial Parfocalization (XRCF)	δX	(μm)	−302	0	+277	−152
Axial Parfocalization (orbit)	δX	(μm)	−42	0	+277	−174
Coma (On-axis)	$Tilt_Y$	(″)	+0.03	−0.02	+0.01	−0.03
Coma (On-axis)	$Tilt_Z$	(″)	−0.09	+0.07	+0.06	+0.32

mirror pair as a whole. Finally, the axial parfocalization was adjusted by modifying the mirror maps (cone-angle adjustments). As further data reduction and analysis takes place and our understanding of the calibration improves, the raytrace model will be refined; ultimately, the raytrace model must be made consistent with the totality of the X-ray and optical calibration datasets.

Further work will be done to improve the 1g mechanical models based on the discrepencies between the XRCF tilt preditions and the HATS optical measurements of coma (§3.1); this will also consider X-ray determined lateral focus information and additional XRCF data such as pinhole raster images.

The calibration AXAF and the assessment of on-orbit performance are ongoing tasks, and the high-fidelity raytrace modeling is an integral component of the calibration effort. The rigid-body mirror parameter measurements as reported in this paper and incorporated into the raytrace model represents a considerable improvement in our knowledge of the HRMA properties.

ACKNOWLEDGEMENTS

We acknowledge the many contributions of the Eastman Kodak Company alignment team; we would particularly like to thank Charlie Atkinson, Greg Hull-Allen, Gary Matthews, and Mark Waldman who were responsible for the success of the HATS alignment system and the alignment of the AXAF optics. Gary Matthews also contributed to our understanding of the 1g effects. Finally, we acknowledge the many contributions of Paul Glenn (Bauer Associates) towards the success of the HRMA alignment.

This work was supported in part by NASA under contract number NAS8–40224.

REFERENCES

1. D. Jerius, M. Freeman, T. Gaetz, J. P. Hughes, and W. Podgorski, "The SAO AXAF simulation system," in *Astronomical Data Analysis and Software Systems*, R. A. Shaw, H. E. Payne, and J. J. E. Hayes, eds., vol. IV, pp. 357–360, 1995.
2. L. Henke, E. M. Gullikson, and J. C. Davis, "X-ray interactions: photoabsorption, scattering, transmission, and reflection at e=50–30,000 ev, z=1–92," *Atomic Data and Nuclear Data Tables* **54(2)**, p. 181, 1993.